

Geometry-Induced Skin Effect in Electron Hydrodynamics

Jarosław Pawłowski  ^{1,*} Piotr Surówka  ^{1,†} and Konstantin Zaremba  ^{2,3,‡}

¹*Institute of Theoretical Physics, Wrocław University of Science and Technology, 50-370 Wrocław, Poland*

²*Nordita, KTH Royal Institute of Technology and Stockholm University, Hannes Alfvéns väg 12, 106 91 Stockholm, Sweden*

³*Niels Bohr Institute, Copenhagen University, Blegdamsvej 17, 2100 Copenhagen, Denmark*

(Dated: January 27, 2026)

In ultra-clean 2d materials electron viscosity is as important as Ohmic dissipation and electron transport exhibits hydrodynamic features. Using a simple framework of Brinkman equations we find that hydrodynamic electron flows exhibit a geometric skin effect: sharp obstacles locally enhance the current suppressing it far from the edges where the flow is unobstructed. This effect arises within hydrodynamic transport with finite momentum relaxation and does not rely on ballistic dynamics. Our results provide a natural hydrodynamic interpretation of edge-enhanced and double-bump current profiles observed in constricted geometries. By comparing with recent scanning NV magnetometry experiments on gated graphene, we demonstrate that such flow patterns are consistent with viscous hydrodynamics shaped by geometry, clarifying the role of geometric effects in the interpretation of electronic flow experiments.

Introduction.—Electron hydrodynamics has emerged as an increasingly important framework for understanding charge transport in ultra-clean conductors. In this regime, momentum-conserving electron-electron collisions dominate over impurity and phonon scattering, allowing the electronic system to behave collectively as a viscous charged fluid [1–14]. Such behavior leads to transport signatures that deviate qualitatively from those expected in the conventional Ohmic or ballistic limits [15–17] (see [18–20] for recent reviews).

Among the various geometries used to probe these effects, constrictions offer a particularly sensitive setting [5, 21]. Unlike extended channels, constrictions reveal flow patterns that strongly depend on the interplay between geometry and microscopic scattering lengths. Recent scanning NV magnetometry experiments on high-mobility graphene have taken advantage of this sensitivity, directly imaging the current distribution as the system crosses over from Ohmic to non-Ohmic transport regimes [8, 11]. A pronounced double-bump profile observed at room temperature gradually evolves into a single-peak structure at lower temperatures, and is commonly interpreted as reflecting a shift in the balance between momentum-relaxing and momentum-conserving scattering. This interpretation implicitly treats the profile shape as a direct diagnostic of the underlying transport regime. As we show below, however, this identification is not unique: similar edge-enhanced structures can arise within a purely hydrodynamic description once the constriction geometry and finite momentum relaxation are taken into account.

Previous theoretical analyses of these experiments have relied primarily on kinetic theory simulations, which provide a detailed and flexible description of the crossover between ballistic, hydrodynamic, and Ohmic regimes. While powerful, such approaches tend to entangle geometric effects with microscopic scattering mechanisms, thereby obscuring the hydrodynamic origin of the observed flow patterns and motivating a more transparent continuum description.

In this work, we develop a simpler, continuum hydrodynamic description based on the Brinkman fluid model [22], which augments the Stokes equation with a finite momentum-

relaxation length. This formulation, similar in spirit to the holographic model of [23], retains the essential ingredients of viscous and Ohmic transport while allowing for transparent analytical treatment of the velocity and potential fields. Following the approach of Falkovich and Levitov [21], the governing equations are solved by Fourier transformation, which reduces the problem to a fourth-order ODE in the transverse velocity. We express the resulting boundary value problem as a singular integral equation for the velocity profile at the constriction, whose structure encodes the transition from narrow-aperture flow to wide-opening behavior and naturally gives rise to the double-bump structure of the current.

To complement this analytical treatment, we also perform direct numerical simulations of the Brinkman–Navier–Stokes equations in constriction and pipe geometries. The flow is modeled in the low-Reynolds-number regime relevant to electronic hydrodynamics, with no-slip boundary conditions at the walls and controlled variation of the momentum-relaxation rate. By systematically varying geometric scales in the problem, we explore the transition from viscous to Ohmic flow and map how the double-bump structure evolves in shape and amplitude.

The numerical solutions confirm the analytical predictions in the low-Reynolds limit and extend them into intermediate regimes that are analytically inaccessible. Together, the analytical Brinkman model and numerical simulations provide a coherent, minimal description of flow through constrictions, capturing both the geometric origin of the observed flow patterns and their evolution under momentum relaxation. This approach offers a transparent physical interpretation and serves as a natural baseline for more elaborate kinetic or microscopic treatments of electronic transport.

Brinkman equations.—Hydrodynamic description of electron transport is a simple extension of Ohm’s law, with a diffusion term representing viscosity of the electronic fluid:

$$-\lambda^2 \nabla^2 j_i + j_i = \sigma \partial_i \varphi, \quad \partial_i j^i = 0. \quad (1)$$

The second equality reflects charge conservation. The Brinkman equation itself describes *spacial dispersion* of con-

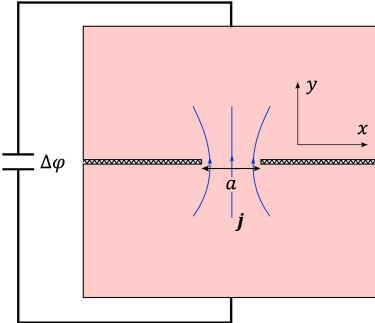


FIG. 1. The flow geometry.

ductivity [24], of a particular form: $\sigma(k) = \sigma/(1 + \lambda^2 k^2)$. The relative importance of viscosity and momentum relaxation is characterized by a length scale λ . In ultra-clean samples the relaxation length can reach up to a few microns making viscosity equally or even more important than dissipation.

In fluid mechanics (1) are known as Brinkman (or Darcy-Brinkman) equations. The Brinkman formulation naturally interpolates between conventional Ohmic flow at $\lambda = 0$ dominated by momentum relaxation and purely viscous Stokes flow at $\lambda \rightarrow \infty$. In the context of electronic hydrodynamics, this corresponds to a crossover between the dissipative Ohmic regime, where momentum relaxes sufficiently fast on the atomic scale and the Gurzhi regime, where electron-electron collisions dominate and momentum is effectively conserved.

Brinkman flow through a constriction: Analytical Results.— The hydrodynamic transport is mostly found in 2d materials, and we focus on a planar, steady-state flow through a constriction of width a , which models typical experimental geometries used in scanning magnetometry and transport measurements. The fluid is injected into an infinite reservoir, parameterized by an upper half-plane $y > 0$, and has a vanishing velocity at infinity (Fig. 1). The following boundary conditions are imposed at $y = 0$:

$$j_i(x, 0) = 0 \quad \text{for } |x| > \frac{a}{2}. \quad (2)$$

We can also set

$$j_x(x, 0) = 0, \quad j_y(x, 0) \equiv J(x) \quad \text{for } |x| < \frac{a}{2}. \quad (3)$$

This is not a boundary condition as the current profile at the aperture $J(x)$ will be determined by the equations themselves.

The linearity of the Brinkman equations suggests to Fourier transform in x , eventually reducing the problem to a fourth-order ODE for the longitudinal component of the current:

$$\left(\frac{\partial^2}{\partial y^2} - k^2 \right) \left(\frac{\partial^2}{\partial y^2} - k^2 - \frac{1}{\lambda^2} \right) j_y(k, y) = 0. \quad (4)$$

Solving this equation together with the boundary conditions (2) and (3) determines the flow profile up to a single unknown

function [25]:

$$j_x = i\lambda^2 J(k) \omega(\omega + |k|) \operatorname{sign} k \left(e^{-\omega y} - e^{-|k|y} \right) \quad (5)$$

$$j_y = \lambda^2 J(k) (\omega + |k|) \left(\omega e^{-|k|y} - |k| e^{-\omega y} \right) \quad (6)$$

$$\varphi = -\frac{\lambda^2 J(k) \omega(\omega + |k|)}{\sigma |k|} e^{-|k|y}, \quad (7)$$

where

$$\omega = \sqrt{k^2 + \frac{1}{\lambda^2}}. \quad (8)$$

Our strategy to determine $J(x)$ exploits the following remarkable observation: the electrostatic potential is the real part of a holomorphic function of the complex variable $z = x + iy$. This is not so for the current components j_i which depend on z and \bar{z} at the same time. The inverse Fourier transform of (7) indeed gives:

$$\varphi(x, y) = \varphi_\infty - \frac{\lambda^2}{\pi\sigma} \operatorname{Re} \int_{-a/2}^{a/2} dx' F(z - x') J(x'), \quad (9)$$

with

$$F(z) = \int_0^\infty dk e^{ikz} \left(k + \frac{1}{\lambda^2 k} + \sqrt{k^2 + \frac{1}{\lambda^2}} \right). \quad (10)$$

The integral nominally diverges at small k . The physical origin of the divergence lies in the momentum dissipation and an infinite extent of the reservoir, a clearly unphysical feature of our simplified setup. The size L of the sample may be large, much bigger than any other scale in the problem, justifying our approximation. The integral is then naturally cut off at the scale $k_{\max} \sim 1/L$ producing a logarithmically large potential difference $\Delta\varphi \sim \ln L/\lambda$ needed to sustain a flow across a big sample. The details of the cutoff procedure are not really important, the divergent constant is simply absorbed into redefinition of φ_∞ .

The potential at the aperture, for $y = 0$ and x between $-a/2$ and $a/2$, cannot depend on x , as any transverse gradient would induce a transverse flow in contradiction to (3). This requirement results in a singular integral equation for the flow profile:

$$\int_{-a/2}^{a/2} dx' G\left(\frac{x - x'}{\lambda}\right) J(x') = C, \quad (11)$$

where C is a constant that determines the overall normalization of the velocity field. The kernel in this equation is the real part of the Green's function (10):

$$G(s) = \frac{2}{s^2} + \ln |s| + \left(\frac{K_1(|s|)}{|s|} - \frac{1}{|s|^2} \right). \quad (12)$$

Integral equations of this type are ubiquitous in random matrix theory, Bethe ansatz and other areas of mathematical physics. A well-developed analytic theory [26, 27] guarantees existence and uniqueness of the solution with zero boundary conditions at the endpoints.

In the limit of no momentum dissipation the midflow has a semicircular profile [28]:

$$J(x) \xrightarrow{\lambda \rightarrow \infty} -\frac{C}{4\pi\lambda^2} \sqrt{a^2 - 4x^2}. \quad (13)$$

This follows easily from the integral equation, by approximating the kernel with the most singular $1/s^2$ term. For the solution to make sense the constant C has to be negative.

Corrections to this solution can be systematically calculated. The first dissipative correction starts at the second order in a/λ and is logarithmically enhanced:

$$J(x) \xrightarrow{\lambda \rightarrow \infty} -\frac{C}{4\pi\lambda^2} \left[1 - \frac{a^2}{64\lambda^2} \left(6 \ln \frac{\lambda}{a} + 7 \ln 4 - 2\gamma + 3 \right) + \frac{x^2}{8\lambda^2} \right] \sqrt{a^2 - 4x^2}, \quad (14)$$

where γ is the Euler constant. The correction is overall negative but uneven: momentum dissipation dampens the current stronger in the middle than at the edges.

The trend continues with growing dissipation and eventually the midflow develops a characteristic double-hump profile seen in the experiment [11]. This is illustrated in Fig. 2 which shows the solution of the integral equation, as well as the current density layout reconstructed from (5) and (6), for different values of the dissipation length. The skin effect is clearly visible for strong enough dissipation, the current then flows primarily near the sharp edges of the constriction. We use the term “skin effect” to denote boundary-localized current enhancement controlled by the Brinkman screening length, which should not be confused with the textbook frequency-dependent suppression of an AC current at the electromagnetic skin depth.

In the limit of very strong momentum dissipation the equation can again be solved analytically. Approximating the kernel by $\ln|s|$ yields the flow profile:

$$J(x) \xrightarrow{\lambda \rightarrow 0} \frac{A}{\sqrt{a^2 - 4x^2}}, \quad A = \frac{2C}{\pi \ln \frac{a}{4\lambda}}. \quad (15)$$

The two humps become infinitely high. An apparent divergence is an artifact of the approximation, in reality the current reaches a maximum of order $j_{\max} \sim C/(\sqrt{a\lambda} \ln(a/\lambda))$ and then relaxes to zero as prescribed by the boundary conditions.

Comparison of the analytic solutions in the two limiting cases reveals an apparent mismatch, with interesting implications for the flow pattern. The solution at small λ requires C to be positive, while at infinite dissipation length this constant must be negative. Hence the two regimes cannot be continuously connected, and there is a phase transition happening in between. Abrupt changes in the flow pattern are ubiquitous in

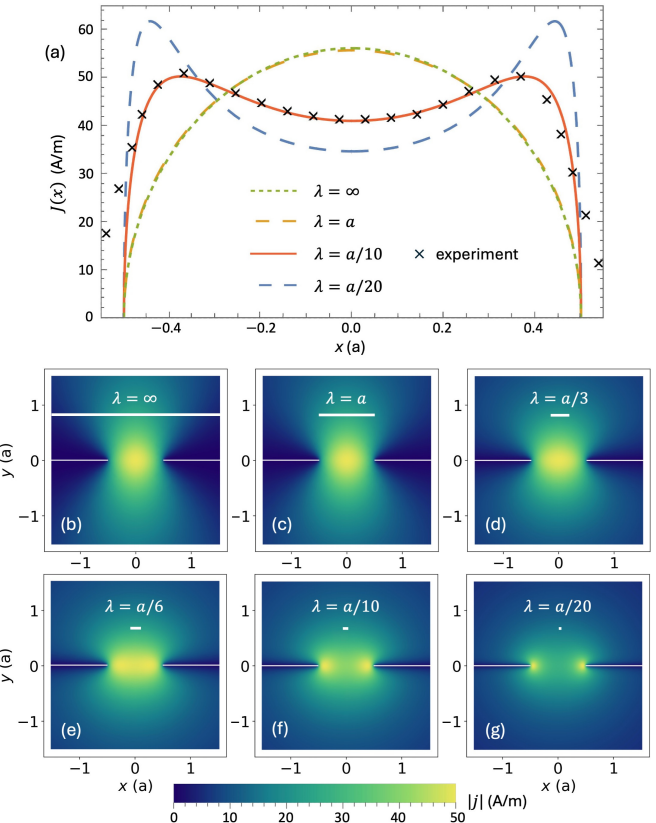


FIG. 2. (a) The flow profile at the aperture compared to the experimental data from [11]. The solid red line is the best fit with $\lambda = a/10$. The dashed lines correspond to $\lambda = a/20$ (blue) as well as $\lambda = a$ (orange) and $\lambda = \infty$ (green) virtually indistinguishable from one another. (b-g) The current density $|j|$ maps for momentum relaxation length $\lambda = \infty, a, a/3, a/6, a/10$, and $a/20$.

hydrodynamics and go under the name of *bifurcations*. Here the bifurcation occurs at $a/\lambda_c = 8.3$ and does not affect much the flow pattern, rather the voltage necessary to sustain the current experiences a finite jump.

Numerical simulations.— For more complex boundary conditions the Brinkman Eq. (1) can be solved numerically using the finite-element method (FEM). As an example we study the flow through a channel of finite width that interpolates between the flow through an infinitely long channel and the geometry we studied so far. Specifically we want to verify if the skin effect survives in a more complicated geometry. In the FEM formulation, the system is modeled as a flow through a pipe with a constriction in a form of perpendicular wall with a channel of a given width a and length l . On the boundaries Γ of the pipe and the constriction wall, we impose no-slip boundary conditions: $j_i(\Gamma) = 0$. Along the aperture (at the center of the channel), we impose a constant potential (φ_0), consistent with the assumptions made for the analytical considerations. A detailed description of the numerical method and the geometry of the computational domain (box) can be found in the Supplementary Materials (SM).

FEM calculations for the shallow channel of length $l =$

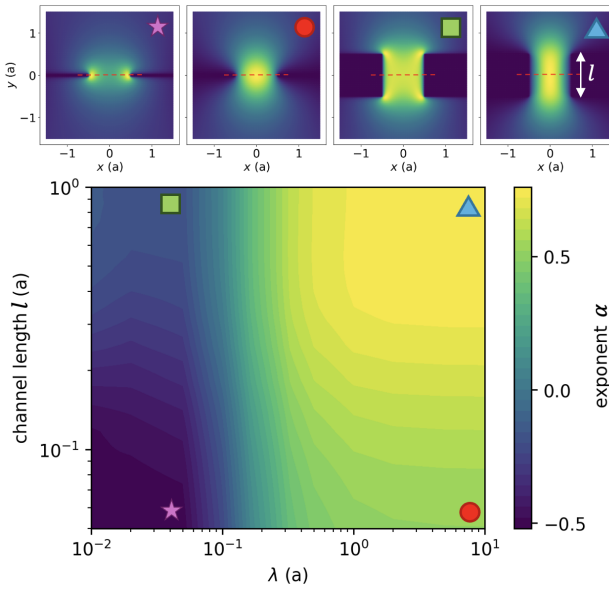


FIG. 3. FEM results for the flow through the channel with a finite length l : maps showing the exponent α fitted to the velocity profile J across the aperture (the fitting line is marked by red dashed lines in the upper panels). Representative cases, with parameter (λ, l) configurations – showing four different flow regimes – indicated by symbols on the map, are shown in the upper panels.

$a/20$ yield very good agreement between the velocity profiles and the analytical results given by Eq. (11). A detailed comparison can be found in SM, confirming the validity of the assumptions made in the analytical considerations. We also extend our results to more realistic geometries with finite-length channels, as presented in Fig. 3. Fitting the current $j_y(x)$ profiles across the channel aperture to the form $A(a^2 - 4x^2)^\alpha$ yields a map of the exponent α , revealing the crossover from the Poiseuille-like profile (with $\alpha > 0.7$ marked by triangle) through the semicircular profile (circle, $\alpha \sim 0.5$), Eq. (13), to the skin-effect profile (star, $\alpha \sim -0.5$). Detailed profile plots can be found in SM. Phase diagram containing viscous, ballistic, and Ohmic regimes of the current profile at a constriction was also discussed in [23]. The Brinkman formulation provides a minimal and analytically tractable description of the viscous-to-Ohmic crossover in constricted geometries, which can be further numerically extended to channels of finite length. The parameter λ controls the spatial decay of the flow and encodes momentum-relaxing processes. In the low dissipation regime $\lambda \gg a$, the current obeys the Stokes flow with the characteristic single-peak Poiseuille-like (long channel) or semicircular profile (narrow channel), whereas for $\lambda \ll a$ the flow approaches the Ohmic limit.

For intermediate and large values of λ/a the flow features a skin effect thereby giving rise to a double-hump structure for the simple single-slit geometry. Such a double-hump profile has been observed experimentally in graphene [11], and our semi-analytic solution shows reasonable agreement with the experimental data for $\lambda \simeq a/10$. Numerical simulation

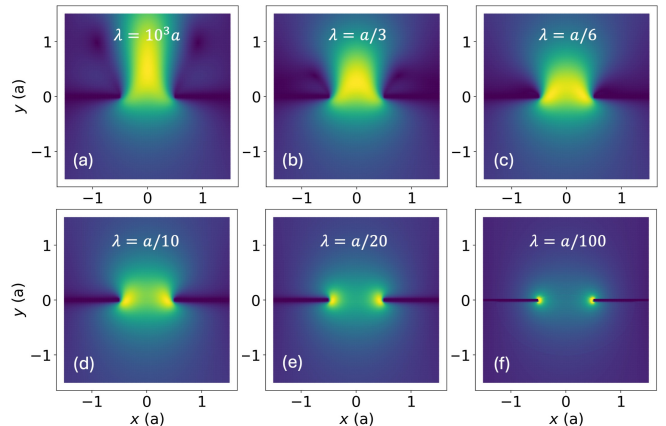


FIG. 4. The current density $|j|$ for various momentum relaxation length λ with a convective term included in the FEM formulation.

of more complex geometries suggest that the skin effect is a universal feature of viscous flows with momentum relaxation, emerging whenever the geometry contains sharp edges. An edge locally enhances the current density, leading to a relative suppression in regions where the flow appears otherwise unobstructed.

The single-slit flow undergoes a bifurcation, a sudden change in the flow pattern under an infinitesimal change of parameters. Bifurcations are common to hydrodynamic flows and by extension should occur in 2d materials with large enough electronic viscosity.

We also studied nonlinear effects by adding convective term $D j_k \partial_k j_i$ to the RHS of the Brinkman Eq. (1) in the FEM formulation. To make convection observable in simulations, we assumed coefficient $D = D_0 = 10^{-6} \text{ m}^2 \text{V/A}^2$ such that for $\lambda = a/10$ convective and Ohmic terms in the aperture area are comparable (see SM for a detailed discussion). One should note, however, that for such large values of D may significantly overestimate convection effects in graphene (by more than a factor of 20, as estimated in SM). Results including the convective term are presented in Fig. 4. They exhibit two characteristic features: (1) the velocity profiles along the aperture, $j_y(y)$, become asymmetric, with the asymmetry reflecting the flow direction; and (2) a characteristic pair of vortices in the j flow emerges in the opening region for slow relaxation (large λ). These are kind of *corner eddies* that emerge due to the presence of neighboring walls of the computational domain, perpendicular to the constriction, with no-slip boundary conditions.

Discussion.—Our results offer a complementary interpretation of current flow profiles observed in constricted graphene geometries, such as those imaged by scanning NV magnetometry. In earlier analyses, double-peaked current profiles were commonly associated with the Ohmic regime dominated by momentum-relaxing scattering, while single-peaked profiles were taken as signatures of ballistic or weakly hydrodynamic transport. Within the Brinkman hydrodynamic framework adopted here, this identification is not unique. We show

that edge-enhanced, double-hump profiles arise naturally in a fully hydrodynamic description once finite momentum relaxation is included, as a consequence of a geometry-induced skin effect. In this picture, the redistribution of current toward sharp edges is not a diagnostic of non-hydrodynamic transport, but rather a generic feature of viscous flow in the presence of dissipation. The constriction geometry thus plays an active role in shaping the flow, and similar profiles can emerge across a broad range of hydrodynamic parameters. Our analysis highlights that current profile shapes alone do not uniquely determine the underlying transport regime, and that geometric effects must be carefully disentangled from microscopic scattering mechanisms when interpreting experiments in constricted electronic systems in analogy with the AC effects [29–31].

Acknowledgements.— We would like to thank C. Arratya, M. Chernodub, G. Falkovich and D. Mitra for very interesting discussions. We also thank M. Chernodub and V. Goy for collaboration on the early stages of this project. P.S. was supported in part by the Polish National Science Centre (NCN) Sonata Bis grant 2019/34/E/ST3/00405. The work of K.Z. was supported by VR grant 2021-04578.

electrons, *Nature* **576**, 75 (2019).

- [8] M. J. H. Ku, T. X. Zhou, Q. Li, Y. J. Shin, J. K. Shi, C. Burch, L. E. Anderson, A. T. Pierce, Y. Xie, A. Hamo, U. Vool, H. Zhang, F. Casola, T. Taniguchi, K. Watanabe, M. M. Fogler, P. Kim, A. Yacoby, and R. L. Walsworth, Imaging viscous flow of the Dirac fluid in graphene, *Nature* **583**, 537 (2020).
- [9] A. C. Keser, D. Q. Wang, O. Klochan, D. Y. Ho, O. A. Tkachenko, V. A. Tkachenko, D. Culcer, S. Adam, I. Farer, D. A. Ritchie, O. P. Sushkov, and A. R. Hamilton, Geometric Control of Universal Hydrodynamic Flow in a Two-Dimensional Electron Fluid, *Physical Review X* **11**, 031030 (2021).
- [10] S. Samaddar, J. Strasdas, K. Janßen, S. Just, T. Johnsen, Z. Wang, B. Uzlu, S. Li, D. Neumaier, M. Liebmann, and M. Morgenstern, Evidence for Local Spots of Viscous Electron Flow in Graphene at Moderate Mobility, *Nano Letters* **21**, 9365 (2021).
- [11] A. Jenkins, S. Baumann, H. Zhou, S. A. Meynell, Y. Daipeng, K. Watanabe, T. Taniguchi, A. Lucas, A. F. Young, and A. C. Bleszynski Jayich, Imaging the Breakdown of Ohmic Transport in Graphene, *Physical Review Letters* **129**, 087701 (2022).
- [12] Z. J. Krebs, W. A. Behn, S. Li, K. J. Smith, K. Watanabe, T. Taniguchi, A. Levchenko, and V. W. Brar, Imaging the breaking of electrostatic dams in graphene for ballistic and viscous fluids, *Science* **379**, 671 (2023).
- [13] M. L. Palm, C. Ding, W. S. Huxter, T. Taniguchi, K. Watanabe, and C. L. Degen, Observation of current whirlpools in graphene at room temperature, *Science* **384**, 465 (2024).
- [14] A. Majumdar, N. Chadha, P. Pal, A. Gugnani, B. Ghawri, K. Watanabe, T. Taniguchi, S. Mukerjee, and A. Ghosh, Universality in quantum critical flow of charge and heat in ultraclean graphene, *Nature Physics* **21**, 1374 (2025).
- [15] R. N. Gurzhi, Minimum of resistance in impurity-free conductors, *JETP* **44**, 771 (1963).
- [16] R. N. Gurzhi, Hydrodynamic effects in solids at low temperature, *Soviet Physics Uspekhi* **11**, 255 (1968).
- [17] R. N. Gurzhi, A. N. Kalinenko, and A. I. Kopeliovich, Electron-electron collisions and a new hydrodynamic effect in two-dimensional electron gas, *Physical Review Letters* **74**, 3872 (1995).
- [18] B. N. Narozhny, Hydrodynamic approach to two-dimensional electron systems, *La Rivista del Nuovo Cimento* **45**, 661 (2022).
- [19] L. Fritz and T. Scaffidi, Hydrodynamic Electronic Transport, *Annual Review of Condensed Matter Physics* **15**, 17 (2024).
- [20] A. Hui and B. Skinner, Hydrodynamics of the electronic Fermi liquid: a pedagogical overview, *Journal of Physics: Condensed Matter* **37**, 363001 (2025).
- [21] L. Levitov and G. Falkovich, Electron viscosity, current vortices and negative nonlocal resistance in graphene, *Nature Physics* **12**, 672 (2016).
- [22] H. C. Brinkman, A calculation of the viscous force exerted by a flowing fluid on a dense swarm of particles, *Flow, Turbulence and Combustion* **1**, 27 (1949).
- [23] X. Huang and A. Lucas, Fingerprints of quantum criticality in locally resolved transport, *SciPost Phys.* **13**, 004 (2022).
- [24] D. B. Tanner, *Optical effects in solids* (Cambridge University Press, Cambridge, UK, 2019).
- [25] K. Zaremba, Joule-Thomson Cooling in Graphene, *JETP Lett.* **111**, 157 (2020).
- [26] F. Gakhov, *Boundary value problems* (Dover Publications, New York, 1990).
- [27] N. Muskhelishvili, *Singular Integral Equations* (Dover Publications, New York, 2013).

- [28] H. Guo, E. Ilseven, G. Falkovich, and L. S. Levitov, Higher-than-ballistic conduction of viscous electron flows, *Proc. Natl. Acad. Sci. USA* **114**, 3068 (2017).
- [29] R. Moessner, P. Surówka, and P. Witkowski, Pulsating flow and boundary layers in viscous electronic hydrodynamics, *Physical Review B* **97**, 161112 (2018).
- [30] R. Moessner, N. Morales-Durán, P. Surówka, and P. Witkowski, Boundary-condition and geometry engineering in electronic hydrodynamics, *Physical Review B* **100**, 155115 (2019).
- [31] P. Cosme, J. S. Santos, and H. Terças, Electronic viscous boundary layer in gated graphene, *Physica Scripta* **97**, 115001 (2022).
- [32] A. J. Chorin, Numerical solution of the Navier-Stokes equations, *Mathematics of Computation* **22**, 745 (1968).
- [33] K. Goda, A multistep technique with implicit difference schemes for calculating two- or three-dimensional cavity flows, *Journal of Computational Physics* **30**, 76 (1979).
- [34] M. Alnæs, J. Blechta, J. Hake, A. Johansson, B. Kehlet, A. Logg, C. Richardson, J. Ring, M. E. Rognes, and G. N. Wells, The FEniCS project version 1.5, *Archive of Numerical Software* **3**, 9 (2015).
- [35] A. Logg and G. N. Wells, DOLFIN: Automated finite element computing, *ACM Transactions on Mathematical Software* **37**, 1 (2010).
- [36] M. S. Alnæs, A. Logg, K. B. Ølgaard, M. E. Rognes, and G. N. Wells, Unified form language: A domain-specific language for weak formulations of partial differential equations, *ACM Transactions on Mathematical Software* **40**, 1 (2014).
- [37] C. Geuzaine and J.-F. Remacle, Gmsh: A 3-D finite element mesh generator with built-in pre- and post-processing facilities, *International Journal for Numerical Methods in Engineering* **79**, 1309 (2009).
- [38] A. Lucas and K. C. Fong, Hydrodynamics of electrons in graphene, *Journal of Physics: Condensed Matter* **30**, 053001 (2018).

Supplementary Material: Geometry-Induced Skin Effect in Electron Hydrodynamics

Finite element calculations in finite domain

To get numerical solutions of the modeled system we use the finite element method (FEM) with a proper variational formulation that gives discretization of the Brinkman equations (1) on the grid that is adapted to the geometry of our problem. In the presented calculations we have used a simple but efficient *splitting method* also known as *Chorin method* [32] or *incremental pressure correction scheme* (IPCS) [33]. To implement the FEM calculations we have used FEniCS library [34, 35] which enables convenient expression of equations in their weak formulation through the UFL language [36]. Meshes were created using the Gmsh library [37].

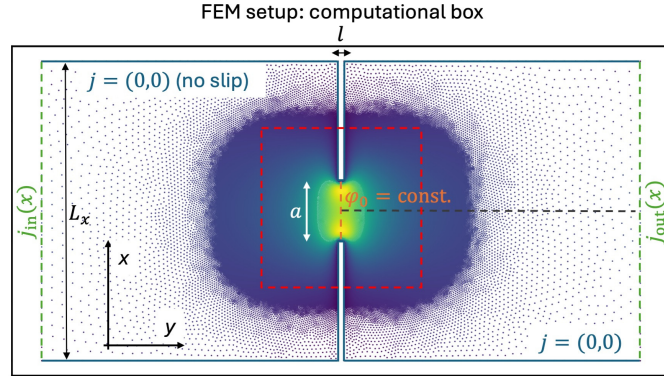


FIG. S1. FEM computational box with marked various boundary conditions.

Let us also comment on two important differences between the problem definition in analytical and numerical domains. Due to the fact that in numerics we have to deal with a finite area, i.e. a computational box that encloses the channel surrounding, in contrast to analytical domain where we solved the equations for infinite half-plane, our numerical formulation resembles rather *Poiseuille flow* through a rectangular pipe with a constriction in a form of a perpendicular wall with a channel of width a and length l . To define a problem in a finite area we have to set up the proper conditions on the computational box boundary as presented in Fig. S1. At the inlet (left side) and outlet (right side) of the pipe (marked by dashed green lines) we impose a Poiseuille flow: $j_{\text{in}}(x) = j_{\text{out}}(x) = (0, j_0(L_x^2 - 4x^2)/L_x^2)$. At the top and bottom edges and on the constriction wall Γ (marked by the blue solid line) no-slip boundary conditions $j_i(\Gamma) = 0$ are enforced. At the center of the channel – across the aperture (marked by the orange dashed line), we impose a constant potential φ_0 . In the vicinity of the channel, the mesh is appropriately

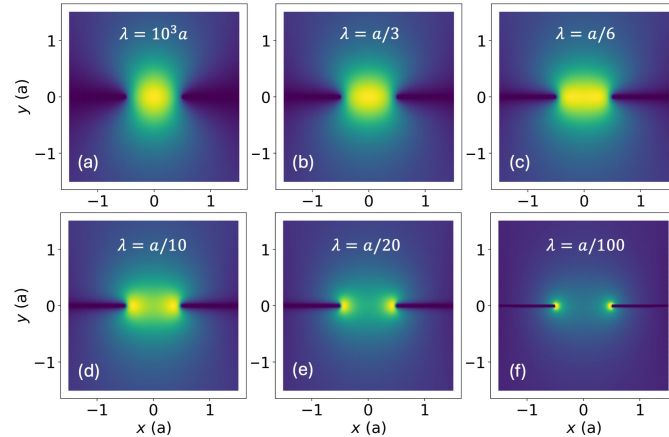


FIG. S2. FEM calculations showing current density $|j|$ for various momentum relaxation length λ .

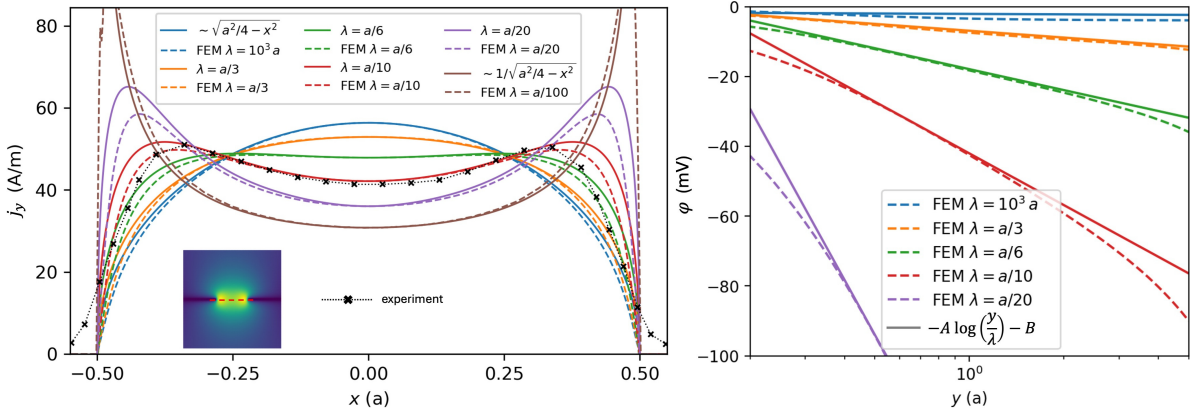


FIG. S3. (left) The longitudinal current $j_y \equiv J$ at midflow (cut section shown in the inset as a red dashed line) comparing analytical solution of the Brinkman equations for an infinitely thin constriction (solid lines) with the numerical FEM solution for the channel of finite length $l = a/20$ (dashed lines). Experimental data (dotted black line) is taken from [11]. (right) Electrostatic potential profiles across the device.

refined to improve numerical accuracy. Fig. S2 displays the current flow in the zoomed-in region marked by the red dashed square in Fig. S1. The results are similar to the analytic solution for the flow in the infinite domain presented in the main text.

To verify approximations used in the analytical considerations, we compare them with the FEM results for the shallow channel of length $l \ll a$. Fig. S3(left) shows comparison between analytical (solid lines) and FEM results (dashed) for the j_y component of the flow, taken along a cut through the channel (orange dashed line in Fig. S1). Small discrepancies can be observed due to the finite channel length, i.e., $l = a/20$. This difference can be controlled by adjusting l , although l must remain nonzero in the FEM formulation. The analytical profiles are normalized so that their central values match the numerical ones. Moreover, our results for $\lambda = a/10$ match the experimental electronic-flow profile in graphene [11], shown as the black dotted line in Fig. S3(left). To fit the experimental profile, we put $j_0 = 13$ A/m.

To verify the logarithmic behavior of the potential at a distance from the constriction, we also present – in Fig. S3(right), FEM results for the potential $\varphi(L_x/2, y)$ along the section depicted in Fig. S1 as black dashed line. Logarithmic fits $-A \log(\frac{y}{\lambda}) - B$ (solid lines) are added to each φ profile (dashed lines) showing approximate logarithmic behavior of the potential in a certain region of the computational box.

Finite channel length

We also introduced FEM to complete the analytical results and extend them on more complex geometries than infinite thin constriction, discussed in Fig. S3. In case of finite channel lengths, for example $l = a$, the profiles are different and presented in Fig. S4. The first important difference is that the double-bump structure can be observed only in the channel outflow area – see Fig. S4(top). In the outflow area – see Fig. S4(bottom left) – we observe transition from semicircular (for large λ) to double-bump (smaller λ) current density profiles. While in the middle of the channel aperture – Fig. S4(bottom right) a Poiseuille (for large λ) or flat (smaller λ) current density profiles are observed. The FEM results (dashed lines) are no longer well reproduced by the analytical results (solid lines), especially in the middle part of the channel. At the opening, the numerical profiles exhibit a certain qualitative agreement with the analytical profiles, derived for infinitely thin constriction.

Convective term

In Fig. S5 we present similar results as in Fig. S3 but now in the FEM formulation a convective term $D j_k \partial_k j_i$ in the RHS of Eq. (1) is included, where $D = \frac{\mu}{v_F^2 e^3 n^2}$ [38]. For typical parameter values [11]: $n = 10^{12}$ cm $^{-2}$, $v_F = 10^6$ m/s, $\mu \approx 0.12$ eV, one finds $D \approx 4 \times 10^{-8}$ m 2 V/A 2 . For estimates $|\mathbf{j}| \sim 50$ A/m and $|\nabla \mathbf{j}| \sim 10^7$ A/m 2 , as in the graphene experiment presented in [11], the convective electric field is $E_{\text{conv}} = D |\mathbf{j}| |\nabla \mathbf{j}| \sim 20$ V/m, while the Ohmic field is $E_{\text{Ohm}} = |\mathbf{j}| / \sigma \sim 500$ V/m (for $\sigma \simeq 0.1$ S/sq). Thus, the convective correction in graphene is of the order of a few percent of the Ohmic term. In the simulations, however, to make convective effects visible, we assume the convective term to have the value $D = D_0 = 10^{-6}$ m 2 V/A 2 , such that for $\lambda = a/10$ in the channel region $E_{\text{conv}} \sim E_{\text{Ohm}}$.

The main effect observed after adding the nonlinear convective term is the emergence of asymmetry in the current-density

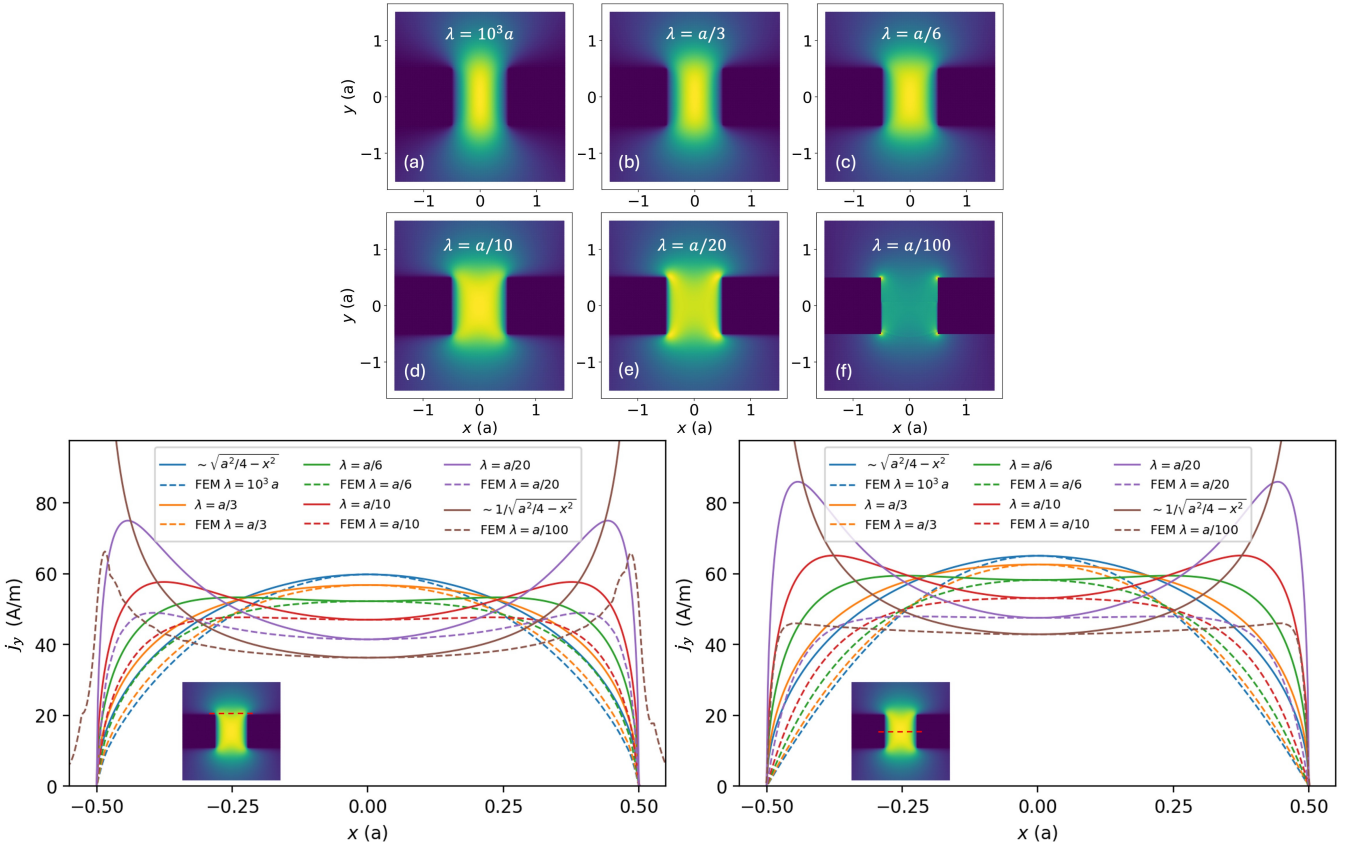


FIG. S4. (top) FEM calculations showing the current density maps $|j|$ for longer channel (of length $l = a$) with increasing momentum relaxation: $\lambda = [10^3, \frac{1}{3}, \frac{1}{6}, \frac{1}{10}, \frac{1}{20}, \frac{1}{100}]a$ for (a-f) subplots, respectively. (bottom) Current j_y component profiles across the channel aperture along two different cut sections: in the channel outflow (left panel) and middle (right panel), shown in respective insets as red dashed sections.

profile along the channel $j_y(y)$, as shown in Fig. 4 in the main text. Moreover, if we examine the profiles $j_y(x)$ across the channel aperture in Fig. S5(left), the inclusion of nonlinear effects causes the flattened, non-Poiseuille-like structure to appear earlier—at larger values of λ than in the case without convection. A similar behavior is observed in Fig. S5(right), where the exponent of the fitted $A(a^2 - 4x^2)^\alpha$ is shown.

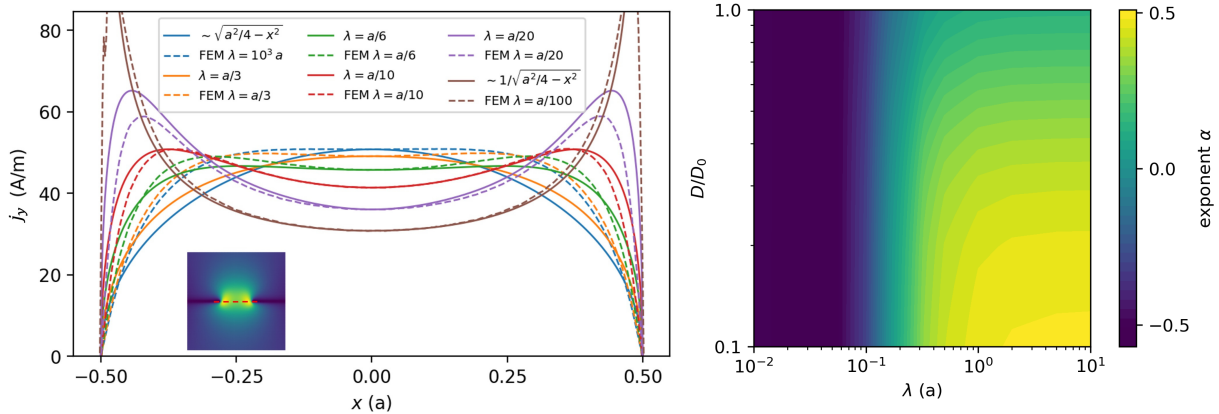


FIG. S5. (left) Same as Fig. S3 but with the convective term included in the FEM calculations. (right) Fitted α exponent, convective case.